Nature Communications

https://doi.org/10.1038/s41467-026-69947-3

Article in Press

Engineering biomimetic chloride channels in ultramicroporous hydrogen-bonded organic framework membranes for high-salinity wastewater valorization

Received: 30 October 2025

Accepted: 13 February 2026

Cite this article as: Zhang, S., Wan, Z., Zhang, X. *et al.* Engineering biomimetic chloride channels in ultramicroporous hydrogen-bonded organic framework membranes for high-salinity wastewater valorization. *Nat Commun* (2026). https://doi.org/10.1038/s41467-026-69947-3

Suixin Zhang, Zongliang Wan, Xu Zhang, Guifeng Liang, Qinshan Zhu, Jin Ran, Peng Cui, Cen-feng Fu, Peipei Zuo & Tongwen Xu

Engineering Biomimetic Chloride Channels in Ultramicroporous Hydrogen-Bonded Organic Framework Membranes for High-Salinity Wastewater Valorization

Suixin Zhang[1#], Zongliang Wan[1#], Xu Zhang[1], Guifeng Liang[2], Qinshan Zhu[2], Jin Ran[1*], Peng Cui[1], Cen-feng Fu[1], Peipei Zuo[2*], Tongwen Xu[2*]

[1] Anhui Key Laboratory of High Value Catalytic Conversion and Reaction Engineering, School of Chemistry and Chemical Engineering, School of Materials Science and Engineering, Hefei University of Technology, Anhui, 230009, P. R. China

[2] State Key Laboratory of Precision and Intelligent Chemistry, School of Chemistry and Material Science, University of Science and Technology of China, Anhui, 230026, P. R. China

Email: ranjin@hfut.edu.cn; zpeipei@ustc.edu.cn; twxu@ustc.edu.cn

[#]Suixin Zhang and Zongliang Wan contributed equally to this work

Abstract

Biological ion channels exemplify nature's high-efficiency ion selectivity filters, yet replicating their functional architectures in synthetic membranes remains a fundamental challenge. Here, we report an ultramicroporous hydrogen-bonded organic framework membrane that structurally emulates the CLC chloride filter. Its channels exhibit size adaptability to anions and incorporate hydrogen-bond donors that provide "low-viscosity" compensatory interactions, thereby alleviating anion dehydration energy penalties. By leveraging differential dehydration and energy compensation between Cl^- and larger anions such as SO_4^{2-}, this bioinspired design achieves an exceptional Cl^-/SO_4^{2-} selectivity of over 400—several tens of times higher than those of existing counterparts—while maintaining a high Cl^- permeation rate double that of the commercial Neosepta® ACS membrane, setting a new benchmark for advanced anion-sieving membranes. In electrodialysis (ED) for high-salinity wastewater valorization, our membrane enables higher NaCl product purity (99.62 wt% vs. 72.86 wt%) with 28.7% lower energy consumption than the Neosepta® ACS membrane. This work establishes a biomimetic design principle of biological anion channels that is potentially extendable to a wide range of selective and conductive membranes.

Introduction

Advanced ion-selective membranes play a vital role in a wide range of water-related applications, including the removal of toxic anions and heavy metal ions in water treatment[1, 2], the production of purified water through desalination[3], and the recovery of valuable resources from high-salinity wastewater[4, 5]. In these processes, the membranes should promote the rapid transport of target ions while effectively excluding others[6]. A typical

example is the Cl^-/SO_4^{2-} separation in the chlor-alkali industry and the NaCl production from hypersaline wastewater, both of which demand membranes that allow efficient Cl^- permeation while strongly impeding the diffusion of SO_4^{2-} [7]. Biological ion channels demonstrate exceptional selectivity and permeation efficiency in nature, and thus have become exemplary models for developing such membranes. A notable case is the CLC family of chloride channels (Fig. 1a), which combine ultrafast Cl^- permeation and exceptional selectivity over competing anions like SO_4^{2-} [8, 9, 10]. This superior performance originates from the collective interplay between the size adaptability of ultramicropore channels and strategically positioned chemical motifs—such as hydroxyl and amino groups—that stabilize partially dehydrated ions via hydrogen bonding[11, 12].

Inspired by the natural blueprint, extensive research has been directed toward designing artificial ion channels using nanostructured materials such as two-dimensional materials (e.g., graphene oxide and MXenes)[13, 14], metal-organic frameworks (MOFs)[15], and covalent organic frameworks (COFs)[16, 17]. These materials provide tunable pore architecture and are often designed with channels rigid in size to improve ion-sieving performance. However, they typically lack the dynamic size adaptability found in biological systems and do not incorporate favorable chemical microenvironments capable of effectively reducing the high-energy barriers associated with ion dehydration, which leads to limited ion permeability. Despite considerable advances, mimicking the sophisticated architecture of biological ion channels remains a fundamental challenge in the development of ion-selective membranes that combine high permeability with precise selectivity[18].

To overcome this challenge, hydrogen-bonded organic frameworks (HOFs) have emerged as a promising membrane material platform due to their unique integration of crystalline porosity, intrinsic framework flexibility, and a high density of hydrogen-bonding sites[19, 20]. These characteristics render HOFs suited to mimic two fundamental principles of biological ion channels (Fig. 1b): (1) size-adaptive ultramicropores that dynamically adjust to translocating ions, and (2) built-in hydrogen-bond donors that compensate for dehydration energy through hydrogen-bond interactions.

Building upon this rationale, we report a biomimetic membrane constructed from a custom-designed HOF composed of diaminotriazole-based two-dimensional molecular sheets, denoted HOF-DAT (Fig. 1c). The membrane contains self-assembled ultramicropore channels that serve as highly efficient artificial chloride channels, closely mimicking the selectivity filter of biological CLC channels. The pores in HOF-DAT membrane undergo adaptive structural swelling to minimize steric hindrance, while the embedded hydrogen-bond donors (–NH– groups) effectively counterbalance the dehydration energy of Cl^-. This engineered architecture delivers: (1) an accelerated Cl^- permeation rate of 3.25 $mol \cdot m^{-2} \cdot h^{-1}$, and (2) a remarkable Cl^-/SO_4^{2-} selectivity of over 400, achieved through distinct dehydration/compensation energy differentiation—performance that surpasses conventional membrane systems. As a result, the HOF-DAT-1 membrane enables the production of high-purity NaCl (99.62 wt%) in treating hypersaline wastewater via a two-stage ED process, combining high selectivity and efficient concentration while reducing energy consumption by 28.7% compared to the commercial Neosepta® ACS membrane.

Results

Biomimetic chloride channel HOF membranes

The HOF-DAT were synthesized via 1,4,5,8-naphthalenetetracarboxylic dianhydride (NTCDA)/diaminotriazole (DAT) condensation (Supplementary Fig. 2)[19], exhibiting favorable solubility in formic acid, facilitating the dissolution recrystallization method for pure HOF membrane fabrication (Fig. 1c

and Supplementary Fig. 3). This method depends on the spontaneous self-assembly of precursors which is driven by two synergistic intermolecular interactions: directional N-H···N hydrogen bonding between adjacent diaminotriazole moieties forms the primary framework architecture; concurrently, the π–π stacking interaction between parallel-aligned naphthalene units provides additional structural stabilization, resulting in a stable three-dimensional framework with openings measuring (W_1) 6.57 × 5.40 Å (Supplementary Fig. 4)[21]. Furthermore, the dislocation-mediated interpore connections generate non-through channels along the Y-direction with the alternating pore of W_2 (size: 6.49 × 4.20 Å) (Fig. 1d). The formation of high-quality membranes with this method relies critically on the simultaneous achievement of extensive nucleation and slow growth rates[22, 23]. Through optimization, we demonstrate that membranes with tunable thicknesses can be synthesized under conditions employing a precursor concentration of 20 $g \cdot L^{-1}$ and a solvent evaporation temperature of 30 °C (Fig. 1e and Supplementary Fig. 5). The successful formation of defect-free membranes across different thicknesses is confirmed by the surface and cross-sectional SEM analyses, revealing compact, pinhole-free microstructures (Fig. 1e and Supplementary Fig. 6). Full characterization details supporting the structural verification of the membranes–including solid-state ^{13}C nuclear magnetic resonance (^{13}C NMR), X-ray photoelectron spectroscopy (XPS), and Fourier-transform infrared (FTIR) spectroscopy–have been documented in Supplementary Information (Supplementary Figs. 7−9)[19, 24].

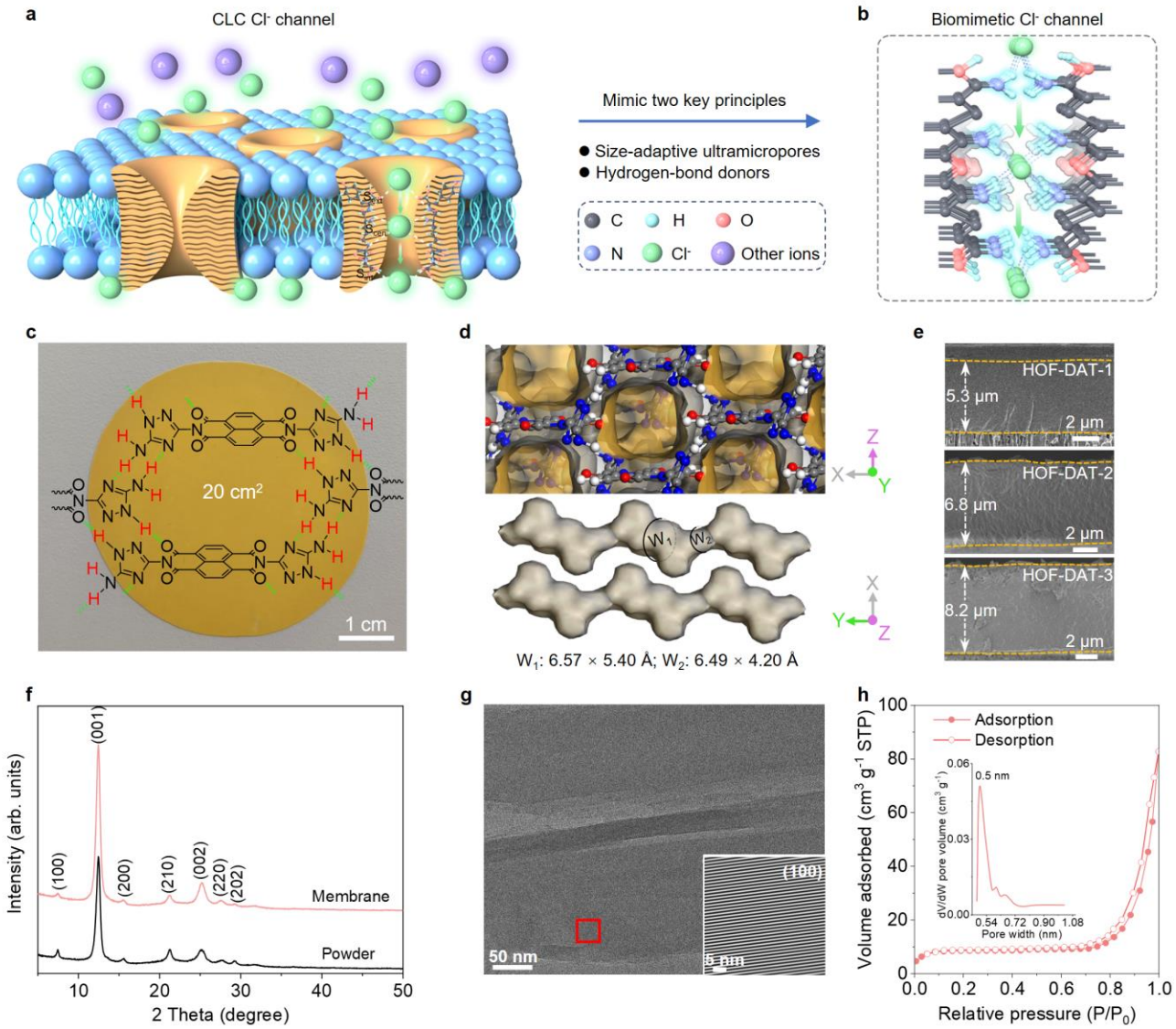

Fig. 1 | Design of HOF membranes with biomimetic chloride ion channels. a, Schematic illustration of the biological CLC Cl^- channel. **b**, Schematic illustration of the biomimetic Cl^- channel structure constructed by HOF. **c**, Digital photograph and molecular structure of the HOF-DAT membrane. **d**, Pore structure diagram of HOF-DAT membrane in different directions. **e**, Cross-section SEM images of HOF-DAT membrane. **f**, XRD patterns of HOF-DAT membrane and its powder form. **g**, HR-TEM image of the HOF-DAT membrane. Inset: the inverse Fast Fourier Transform lattice image of the area in red. **h**, N_2 adsorption isotherms of HOF-DAT membrane at 77 K and Horvath-Kawazoe pore size distributions.

We hypothesize that the three-dimensional frameworks in HOF-DAT membranes, formed by synergistic dynamic hydrogen bonds and π–π stacking, would concurrently deliver thermodynamic stability, structural crystallinity, and porosity. This is supported by the thermogravimetric analysis of the membrane, which reveals a high decomposition onset temperature above 450 °C (Supplementary Fig. 10). Besides, the crystalline integrity is confirmed by XRD, demonstrating that the membrane's diffraction pattern closely matches that of its powdered form. Distinct peaks at 7.45°, 12.44°, 15.49°, 21.27°, 25.23°, 27.6°, and 29.12° can be assigned to the (100), (001), (200), (210), (002), (220), and (202) crystallographic planes, respectively (Fig. 1f)[25]. Notably, the

HOF-DAT membrane demonstrates excellent structural stability following 100 days of immersion in a 1 mol·L^{-1} mixed salt solution ($NaCl/Na_2SO_4$). As shown in Supplementary Fig. 11, the XRD patterns before and after immersion are highly consistent, with all characteristic diffraction peaks retaining their original positions and intensities and no new peaks appearing. These results confirm that the crystalline structure and long-range order of HOF-DAT remain intact after prolonged salt exposure, without detectable degradation, phase change, or swelling. The membrane also demonstrates excellent acid–base resistance, maintaining its structural integrity without significant changes in crystalline structure or chemical composition over 20 days across a wide pH range of 2-11 (Supplementary Fig. 12). This hydrolytic and acid-base stability provides a solid structural foundation for long-term membrane performance evaluation. The crystalline structure of the HOF-DAT membrane is further validated by high-resolution transmission electron microscopy (HR-TEM), revealing well-defined lattice fringes with periodicity along the [100] crystallographic direction (Fig. 1g and Supplementary Figs. 13−14). Nitrogen adsorption-desorption analysis (Fig. 1h) confirms the porosity of the HOF-DAT membrane, revealing a predominant pore size of 0.5 nm (a value consistent with that measured by the crystallographic model, Fig. 1d).

Anion separation performance of HOF membranes

Based on the transport number assessment, the HOF-DAT membrane is determined to be an anion-preferential material, with selectivity ratios of 2.5 for Cl^-/K^+, 3.7 for Cl^-/Na^+, and 26.8 for Cl^-/Ca^{2+} (Supplementary Fig. 15). To further assess its anion transport performance, we measured the permeability of anions with varied hydration size (Supplementary Table 1) through the HOF-DAT membrane using a two-chamber diffusion cell (Fig. 2a). The concentration-driven diffusion experiment employed 0.5 mol·L^{-1} salt as feed solutions, with the ion permeation rate monitored through conductivity measurements. The permeation rates of larger anions (SO_4^{2-}, and WO_4^{2-}) are approximately two orders of magnitude lower than those of monovalent species (Supplementary Fig. 16), demonstrating the great potential of HOF-DAT membranes for efficient separation of mono-/divalent anions. We then used the Cl^-/SO_4^{2-} sieving model system and quantified selective anion transport. As expected, increasing membrane thickness from 5.3 μm to 8.2 μm induces a reduction in Cl^- permeation rate (from 2.44 to 1.41 mol·m^{-2}·h^{-1}), while yielding an enhanced ideal Cl^-/SO_4^{2-} selectivity which escalates from 152.5 to 197 (Supplementary Fig. 17). This inverse correlation between ion permeation rate and selectivity aligns with the classic trade-off behavior in membrane science[26, 27], yet critically, in terms of both Cl^- permeation rate and selectivity, HOF-DAT membranes significantly outperform other typical anion-selective analogues such as imine-based COFs (Cl^- permeation rate: 0.09 mol·m^{-2}·h^{-1}; selectivity: 62; Supplementary Fig. 18 and Table 2). Furthermore, the HOF-DAT-1 membrane demonstrates operational stability, maintaining consistent performance over 20-hour continuous testing (Supplementary Fig. 19).

Building on these findings, we evaluated HOF-DAT membrane performance in a binary Cl^-/SO_4^{2-} mixed solution. The membranes maintain their sieving behavior observed in single-salt systems (Fig. 2b), except that both ion permeation rate and selectivity show about 10%–20% reductions. This reduction is primarily attributed to competitive ion coupling in the mixed-salt system[16, 28, 29]. Specifically, the kinetic trapping and transient accumulation of SO_4^{2-} at channel entrances not only sterically hinder Cl^- transport but also elevate its permeation energy barrier by altering the local electrostatic environment, thereby accounting for the diminished selectivity relative to the single-salt case[16]. We then subjected the HOF-DAT-1 membrane–identified as a good performer through its balanced Cl^- permeation rate (2 mol·m^{-2}·h^{-1}) and Cl^-/SO_4^{2-} selectivity (137)–to operational stability testing by both 100-cycle intermittent testing and continuous 60-hour operation (Fig. 2d, Supplementary Fig.

20). As expected, this membrane demonstrated excellent structural integrity throughout these evaluations, as evidenced by SEM micrographs, and XRD patterns acquired before and after testing (Supplementary Figs. 21−22). Moreover, the HOF membrane maintains stable ion sieving performance across varying pH levels (2-11), demonstrating membrane's potential for use in real wastewater environments with fluctuating pH (Supplementary Fig. 23). Interestingly, the HOF-DAT-1 membrane also exhibits superior performance in separating other monovalent anions—such as F^-, Br^-, and NO_3^- from SO_4^{2-} (Fig. 2c). For instance, it achieves a high F^-/SO_4^{2-} selectivity of 108 and an F^- permeation rate of 1.62 $mol \cdot m^{-2} \cdot h^{-1}$, significantly surpassing the Neosepta® ACS membrane (F^- permeation rate of 1.15 $mol \cdot m^{-2} \cdot h^{-1}$, selectivity of only 1.4)[30]. This broad-spectrum monovalent selectivity aligns with the behavior of biological CLC channels, which effectively transport anions similar in size to Cl^- while impeding the passage of multivalent ions (Supplementary Fig. 24)[8, 9, 10].

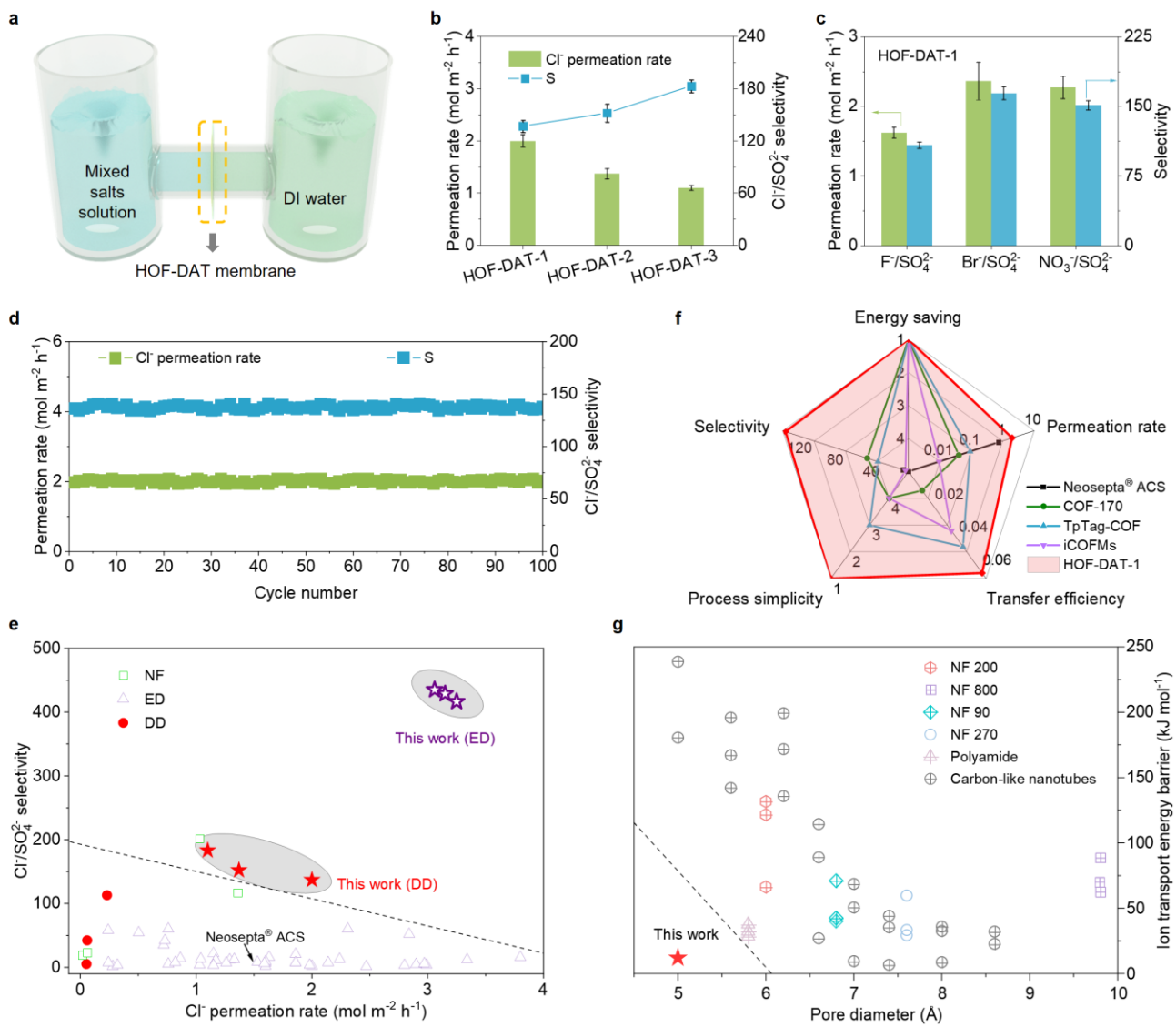

Fig. 2 | Anion separation performance of HOF membranes. a, Schematic diagram of a diffusion dialysis (DD) unit. **b**, Cl^- permeation rate and Cl^-/SO_4^{2-} selectivity of HOF-DAT membranes in 0.5 $mol \cdot L^{-1}$ $NaCl/Na_2SO_4$ binary-salt solution. **c**, Ion

permeation rate and selectivity of the HOF-DAT-1 membrane in different mixed salt solutions. **d**, Cyclic stability of the HOF-DAT-1 membrane. **e**, Comparison of Cl^-/SO_4^{2-} separation performances between HOF-DAT membranes and literature-reported membranes[16, 17, 31, 32, 33, 34, 35, 36, 37, 38, 39, 40, 41, 42, 43, 44, 45, 46, 47, 48, 49, 50, 51]. **f**, Radar plot comparing the comprehensive characteristics of the HOF-DAT-1 and reported membranes[16, 17, 35, 52] (The data acquired for the HOF-DAT-1 membrane operating in the DD mode were employed as a benchmark). **g**, Comparisons of the ion transport energy barrier of the HOF-DAT-1 membrane with literature-reported membranes and channels across varying pore diameters[53, 54, 55, 56]. Error bars represent the mean ± SD, n = 3.

A comparison against established Cl^-/SO_4^{2-} separation technologies—including DD, ED, and nanofiltration (NF)—confirms the superior performance of HOF-DAT membranes in combining high Cl^- permeation with exceptional selectivity (Fig. 2e). Specifically, in the DD configuration, these membranes achieve a Cl^- permeation rate 1-2 orders of magnitude greater (1-2 $mol \cdot m^{-2} \cdot h^{-1}$) than reported benchmarks while maintaining a high Cl^-/SO_4^{2-} selectivity of >130. Remarkably, under ED conditions, the HOF-DAT membranes deliver dramatically enhanced Cl^-/SO_4^{2-} selectivity of >400—representing a ~50-fold improvement over the Neosepta® ACS membrane—while also maintaining a higher Cl^- permeation rate (>3.0 vs. 1.53 $mol \cdot m^{-2} \cdot h^{-1}$) (Supplementary Fig. 25 and Table 3). This combination of properties places them among the top-performing membranes reported to date (Fig. 2e). This outstanding performance in Cl^-/SO_4^{2-} separation, combined with a simple membrane fabrication process and energy saving, positions the HOF-DAT-1 membranes as promising candidates for anion separation, outperforming other typical membranes (Fig. 2f, and Supplementary Table 4). More notably, the HOF-DAT-1 membrane shows an ultralow apparent activation energy of 12 $kJ \cdot mol^{-1}$ for Cl^- transport (Supplementary Figs. 26–29)—among the smallest reported for subnanometer channels. This value is especially notable given the membrane's ~0.5 nm constricted pores, which conventionally impose high energy barriers to ion transport[53, 54, 55, 56] (Fig. 2g, and Supplementary Table 5).

Size-adaptive channels and hydration compensation for anion transport

To elucidate the origin of the exceptionally low Cl^- transport barrier in narrow-pore HOF-DAT membranes, we first investigated ion dehydration dynamics through radial distribution function (RDF) analysis of ion-hydrogen of water (H_W: H in water). These simulations reveal that Cl^- requires the shedding of 3 water molecules from their primary hydration shell during pore entry, while SO_4^{2-} necessitates the removal of 6.8 hydration waters (Supplementary Fig. 30). These dehydration values are much lower than those observed in rigid 0.5 nm artificially simulated channels (6 and 12.4 water molecules removed for Cl^- and SO_4^{2-}, respectively, Supplementary Fig. 31). This contrast is anticipated to stem from HOF's size adaptability in regulating ion dehydration energies during ion transport. The size adaptability was experimentally verified through in situ XRD characterization of HOF-DAT-1 membrane under various ionic conditions (NaCl, NaF, NaBr, $NaNO_3$, Na_2SO_4, Na_2WO_4, and $Na_4[Fe(CN)_6]$ solutions). As shown in Supplementary Fig. 32, exposure to anions with hydrated diameters below 7.86 Å induces measurable low-angle shifts (0.1°–0.4°) in characteristic diffraction planes, suggesting a transient lattice expansion. In contrast, the treatment with larger $Fe(CN)_6^{4-}$ ions (hydrated diameter 8.44 Å) left the diffraction pattern unchanged, indicating its exclusion from the membrane pores. Complementary molecular dynamics (MD) simulations further demonstrate this size-dependent accessibility, revealing Cl^--induced pore dilation. Specifically, the framework apertures dynamically adapt during Cl^- transit, with W_1 and W_2 varying by 0.04 × 0.17 Å and 2.52 × 0.77 Å, respectively, relative to the pristine state. Similar pore expansion phenomena—to varying degrees—are observed with other anions, further verifying the occurrence of differentiated dynamic pore adaptation (Figs. 3a–3b and Supplementary Fig. 33).

While the intrinsic size flexibility of HOF pores helps reduce ion transport resistance, this adaptability alone cannot explain the remarkably low apparent energy barrier for Cl^- permeation—especially given the significant dehydration energy needed to displace three coordinated water molecules[56]. We speculate that energy penalties associated with dehydration can be mitigated by the HOF's abundant H-bond donor sites (denoted as H_N: H on the NH_2 of HOF-DAT), which compensate for lost H_W interactions. This compensation mechanism can be validated by the MD simulations (Figs. 3c–3f). Cl^- entering size-adaptive pores experiences replacement of 2.9 H_W interactions with 2.9 H_N interactions from the framework, preserving its total coordination number (H-bond count) during transit. In contrast, SO_4^{2-} exhibits only partial compensation, forming just 3 H_N interactions while leaving 3.8 H_W interactions uncompensated (Fig. 3g, and Supplementary Fig. 34).

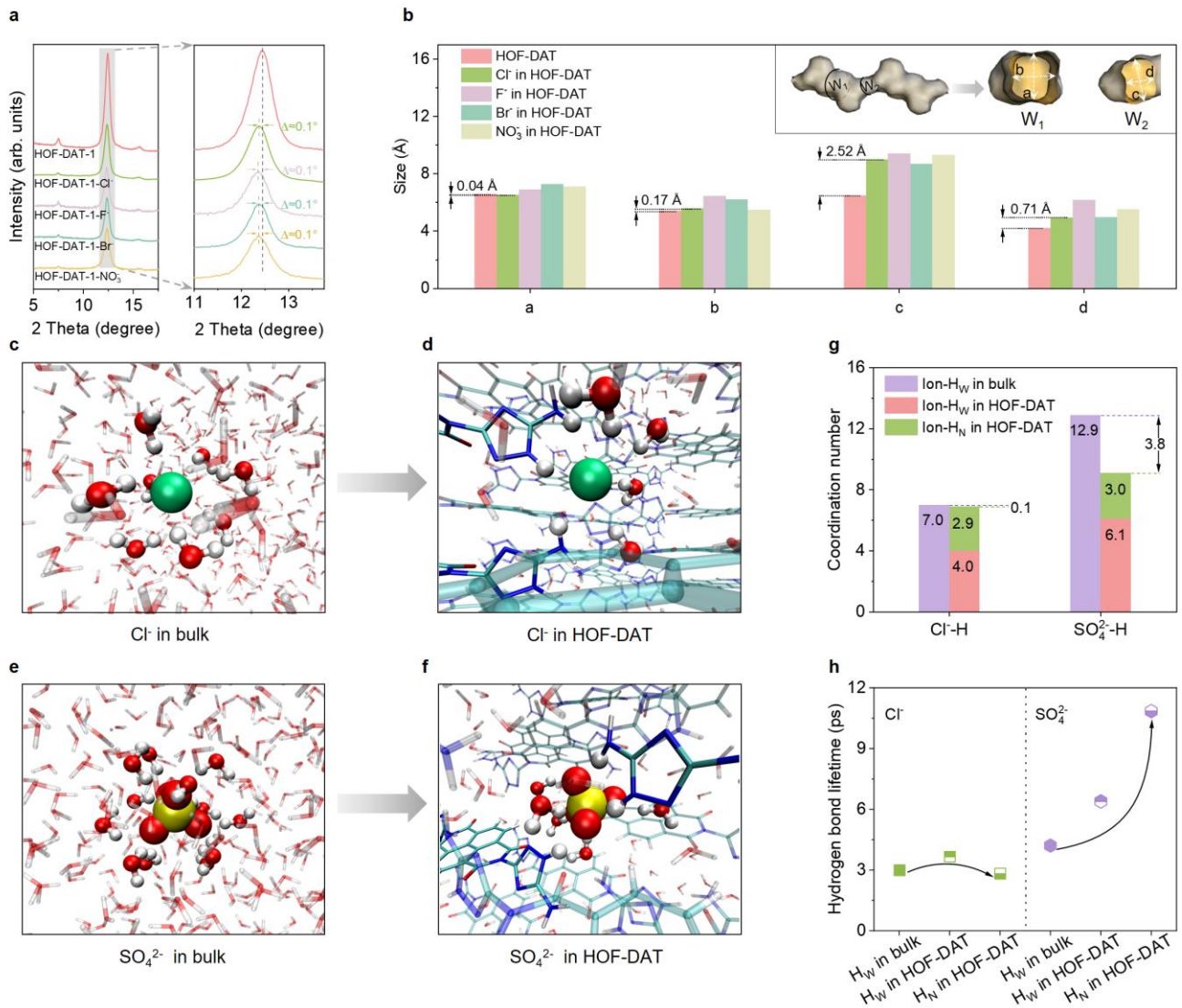

Fig. 3 | Mechanism of anion transport and separation. a, XRD patterns of the HOF-DAT-1 membrane upon immersion in solutions containing different anions. **b**, Anion transport-induced pore size changes in the HOF-DAT membrane. Insert: schematic of the pore structure, where for descriptive purposes, the parameters a and b represent the pore dimensions of W_1 along different directions, while c and d represent those of W_2. **c-f**, Snapshots of the first hydration shell of the ions from a 50 ns MD simulation at 300 K: Cl^- and SO_4^{2-} in bulk solution and HOF-DAT. Water molecules in the first hydration shell are shown in Corey-Pauling-

Koltun (CPK) representation, with the remaining waters as licorice. HOF-DAT are shown in licorice representation, with cyan, red, navy, and white representing carbon, oxygen, nitrogen, and hydrogen atoms, respectively. For clarity, hydrogen atoms from HOF-DAT's NH_2 groups participating in the first hydration shell are represented by white spheres. Ions are shown as van der Waals (vdW) spheres, with green for chlorine (Cl^-) and yellow for sulfur (in SO_4^{2-}). **g**, Hydrogen coordination number in the first hydration shell of the ions: provided by water molecules (H_W) in bulk solution, and by both water molecules (H_W) and NH_2 groups (H_N) in HOF-DAT (The coordination number reported here is defined based solely on spatial proximity, considering hydrogen atoms located within the first hydration shell of the ion). **h**, Hydrogen bond lifetime of Cl^--H and SO_4^{2-}-H in bulk and HOF-DAT.

We next performed an advanced hydrogen-bond lifetime analysis by calculating hydrogen-bond correlation functions from MD simulations[57] to quantify the temporal stability of three distinct interaction types: (1) ion-H_W in bulk solution, (2) ion-H_W within HOF-DAT pores, and (3) ion-H_N within HOF-DAT pores (Fig. 3h, and Supplementary Fig. 35). SO_4^{2-} is found to exhibit prolonged H-bond stabilization within HOF-DAT channels, displaying an average interaction lifetime of 10.85 ps-3.8 times longer than Cl^- (2.84 ps). Furthermore, the hydrogen bond lifetime of Cl^--H_N within the HOF-DAT pores is slightly shorter than that of Cl^--H_W in bulk solution (3.01 ps). This dramatic disparity arises from SO_4^{2-}'s higher charge (-2 vs. Cl^-'s -1), which enhances its binding affinity to both residual H_W and framework H_N groups[58, 59]. The extended H-bond lifetime creates a kinetic bottleneck, effectively increasing SO_4^{2-}'s residence time, in contrast to Cl^-, which enables rapid coordination water exchange facilitating translational motion[60]. In all, Cl^- achieves ultralow-energy transport through size-adaptive channels via near-complete hydration compensation and rapid ligand exchange, while stark disparities in hydration dynamics (3 vs. 6.8 H_2O shed; 96.7% vs. 44.1% hydrogen bond compensation efficiency) and H-bond lifetimes (2.84 vs. 10.85 ps) between Cl^- and SO_4^{2-} contribute to their high selectivity.

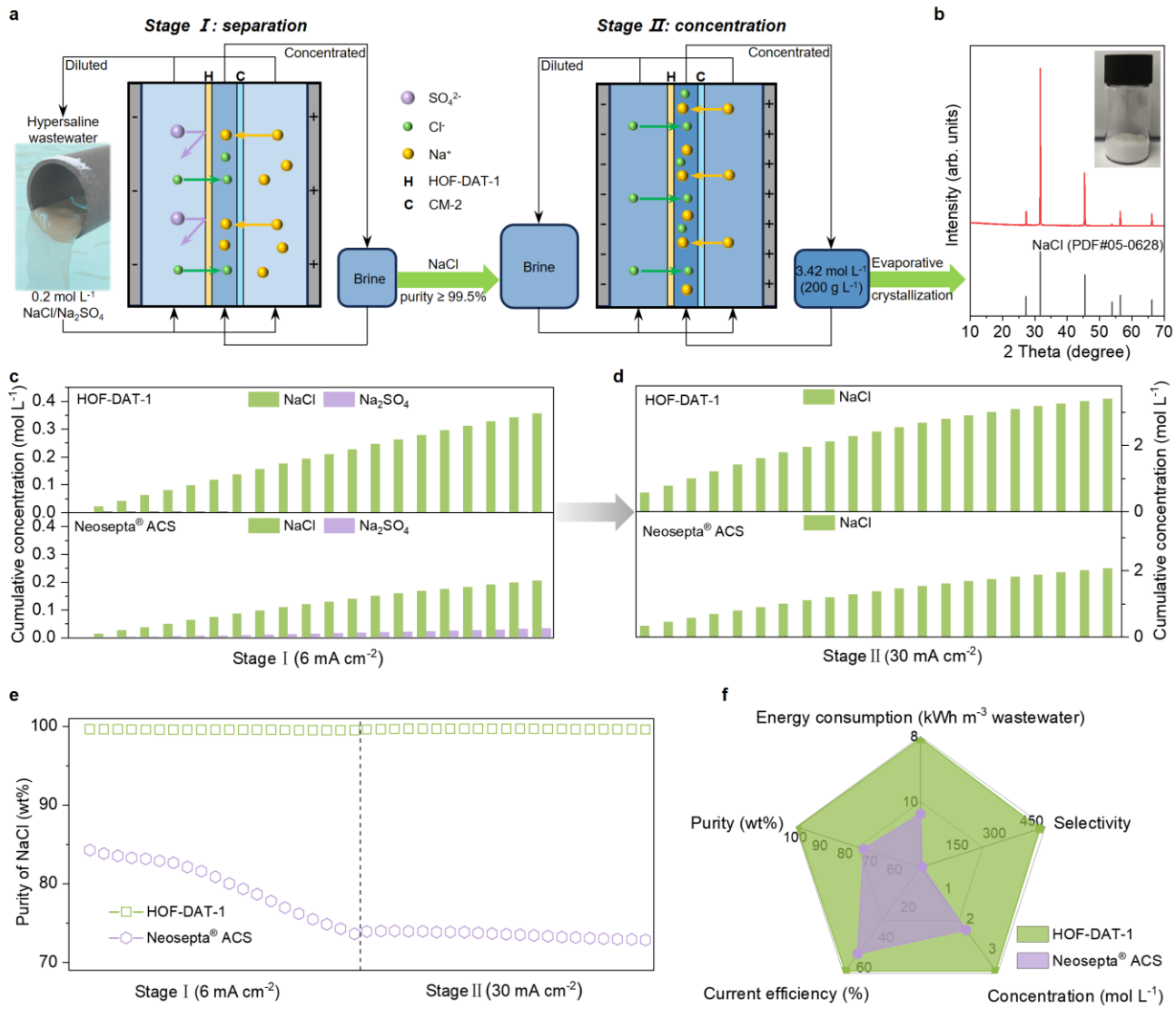

Fig. 4 | Demonstration of high-salinity wastewater valorization via ED. a, Schematic diagram of the two-stage ED process. The performance of the ED cell with HOF-DAT-1 was evaluated, with the Neosepta® ACS membrane as the control sample. **b**, XRD pattern of the NaCl product collected after the ED assembled with HOF-DAT-1, confirming its high purity by a complete match with the standard reference. The inset shows a photograph of the final NaCl products. **c**, **d,** Evolution of NaCl and Na_2SO_4 concentrations in the concentrate during two-stage ED: (**c**) first-stage at 6 mA·cm^{-2} for separation, and (**d**) second-stage at 30 mA·cm^{-2} for concentration. **e**, Evolution of NaCl purity in the concentrate during two-stage ED. **f**, Radar plot comparing the comprehensive characteristics of HOF-DAT-1 and Neosepta® ACS membranes.

HOF membranes addressing resource utilization of hypersaline wastewater

The high performance of our HOF membranes in selectively transporting anions is exemplified using a two-stage ED process (Fig. 4a, and Supplementary Fig. 1), which is critical for industrial NaCl purification. This system supports zero-liquid discharge and resource utilization of hypersaline wastewater generated in coal chemistry, pharmaceutical industry, and dye industry[61, 62]. By leveraging the membrane's high Cl^-/SO_4^{2-} selectivity, the process extracts Cl^- from mixed anions in sequential separation and concentration stages, enabling

the production of high-purity NaCl (Fig. 4b). In the first separation stage, conducted at 6 $mA \cdot cm^{-2}$, the NaCl concentration in the concentrate chamber increases steadily by 0.35 $mol \cdot L^{-1}$ for the HOF-DAT-1 membrane (Fig. 4c, upper panel), while maintaining a high purity exceeding 99.5 wt% (Fig. 4e). Moreover, after prolonged operation, the membrane exhibits no significant fouling or swelling, with its structure and ion-sieving performance remaining stable (Supplementary Fig. 40). In contrast, the Neosepta® ACS membrane exhibits a significant decline in NaCl purity to 73.6 wt% after this stage (Fig. 4e), which is attributed to substantial SO_4^{2-} co-permeation alongside Cl^- (Fig. 4c, bottom panel). During the second concentration stage, the current density of 30 $mA \cdot cm^{-2}$ was applied to accelerate NaCl enrichment. With the HOF-DAT-1 membrane, this step produces a final NaCl concentration of 3.42 $mol \cdot L^{-1}$ with 99.62 wt% purity (Figs. 4d−4e), making the product suitable for crystallizer feed (Fig. 4b)[61]. Under identical conditions, the Neosepta® ACS membrane only reaches a NaCl concentration of 2.07 $mol \cdot L^{-1}$ with a purity of approximately 72.86 wt% (Figs. 4d−4e). The HOF-DAT-1 system thus reduces energy consumption by 28.7% compared to the Neosepta® ACS membrane (1.27 vs. 1.78 $kWh \cdot kg^{-1}$ of NaCl). Based on our measurements, the HOF-DAT membrane consumes approximately 8.06 $kWh \cdot m^{-3}$ when treating high-salinity wastewater—a value higher than that of reverse osmosis/nanofiltration technologies used for low-salinity desalination, yet significantly lower than thermal evaporation processes, while being competitive with the lower end of the energy consumption range for electrically-driven salt separation technologies[5, 63]. This was calculated from the energy required per kilogram of NaCl recovered. A preliminary techno-economic analysis (TEA) further estimates the total processing costs at about \$1.68 m^{-3} for Stage I and \$0.95 $\cdot m^{-3}$ for Stage II, respectively (Supplementary Table 6)[64, 65]. The overall superiority of the HOF-DAT-1 membrane in high-purity NaCl production is further demonstrated in the radar chart comparing key performance metrics, including current efficiency, NaCl purity, energy consumption, selectivity, and final NaCl concentration (Fig. 4f).

Discussion

Through mimicking the architecture of CLC chloride channels, we designed a HOF-DAT membrane featuring size-adaptive, hydrogen-bonded ultramicropore channels. This membrane significantly mitigates the classical permeability–selectivity trade-off for anion separation. Specifically, these channels can tune ion-specific dehydration processes through the "guest size-adaptive effect" (i.e., undergoing differentiated dynamic size adjustments in response to varying guest ions), leading to a small number of stripped water molecules for small ions but larger dehydration numbers for larger ions (small ions like Cl^- shed only 3 water molecules versus 6.8 for SO_4^{2-}). Concurrently, precisely aligned hydrogen-bonding sites create a "low-viscosity" microenvironment with weak coordination bonds that perfectly stabilize partially dehydrated Cl^- with the coordination number in alignment with the dehydration stoichiometry while mismatching SO_4^{2-} hydration states. This dehydration/compensation-energy differentiation process enables Cl^- transport with ultralow energy barriers of 12 $kJ \cdot mol^{-1}$ and records Cl^-/SO_4^{2-} selectivity of over 400. When applied in a two-stage ED process for high-purity NaCl production, the HOF-DAT-1 membrane achieves high-purity NaCl (99.62 wt%) with 28.7% lower energy consumption than the commercial Neosepta® ACS membrane. This work not only demonstrates HOFs as a promising platform for constructing artificial ion channels but also establishes a paradigm for the rational design of next-generation separation membranes through bioinspired microenvironment engineering.

Methods

Synthesis of HOF-DAT

A total of 198.2 mg (2 mmol) of DAT was dissolved in 20 mL of dimethylacetamide (DMAc) under a nitrogen atmosphere while maintaining an ice bath. Subsequently, 268 mg (1 mmol) of NTCDA was added to the solution, and the mixture was stirred until a clear yellow solution formed. Following this, an additional 50 mL of DMAc was incorporated to dilute the reaction mixture, and the mixture was stirred in the ice bath for 30 minutes. The resulting mixture was then transferred into a 100 mL Teflon-lined autoclave and subjected to heating at 180 °C for 10 hours. Upon completion of the reaction and cooling to room temperature, the solid product was collected by centrifugation at 9576 g for 15 minutes. The solid was subsequently washed sequentially with dimethylformamide (DMF), anhydrous methanol, and deionized water. After freeze-drying for 48 hours, 310.9 mg of the product was obtained (72.3% yield).

Fabrication of HOF-DAT membranes

The HOF-DAT membranes were prepared using the dissolution-recrystallization method. HOF-DAT was dissolved in formic acid to create an HOF-DAT solution with a concentration of 20 $g \cdot L^{-1}$. Subsequently, the HOF-DAT membrane was fabricated via the solution casting method. Herein, to prepare sufficiently thin membranes, the polycarbonate (PC) substrate was employed as the support. The solvent was then evaporated at 30 °C (a low temperature to allow slow recrystallization) for 6 hours to yield a continuous yellow HOF-DAT membrane. Finally, the HOF-DAT membranes were activated at 80 °C for 12 hours. Different thicknesses of HOF-DAT membranes can be achieved by varying the volume of the HOF-DAT solution.

Evaluation of the ion separation performance of HOF-DAT membranes

Single ion separation performance (DD): HOF-DAT membranes were affixed to the center of the copper tape and secured to the DD test device. Each membrane had an effective area of 0.5 cm^2. One side of the membrane faced a chamber containing 100 mL of single-salt solutions with a concentration of 0.5 $mol \cdot L^{-1}$ for NaCl, NaF, NaBr, $NaNO_3$, Na_2SO_4, Na_2WO_4, and $Na_4Fe(CN)_6$. The opposite side faced another chamber containing 100 mL of deionized water, referred to as the diffusion chamber. Continuous stirring was maintained throughout the experiment to minimize the effects of concentration polarization. After 1 hour, we measured the conductivity of the solution on the diffusion side and calculated the concentrations of monovalent and divalent ions based on the established standard curve correlating various solution concentrations with their respective conductivities.

Binary-ion separation performance (DD): HOF-DAT membranes were affixed to the center of the copper tape and secured to the DD test device. Each membrane had an effective area of 0.5 cm^2. One side of the membrane faced a chamber containing 100 mL of mixed salt solutions with a concentration of 0.5 $mol \cdot L^{-1}$ for $NaCl/Na_2SO_4$, NaF/Na_2SO_4, $NaBr/Na_2SO_4$, or $NaNO_3/Na_2SO_4$. The opposite side faced another chamber containing 100 mL of deionized water, referred to as the diffusion chamber. Continuous stirring was applied throughout the experiment to minimize the effects of concentration polarization. After 1 hour, a small sample of the solution on the diffusion side was extracted, and the ion concentration was analyzed using ion chromatography.

Binary-ion separation performance (ED): based on the results of previous DD experiments, ED tests were conducted to further evaluate the ion sieving performance of the selective HOF-DAT-1 membrane. A four-compartment ED setup was employed to assess the anion transport rate and selectivity of the membrane. The

tested membrane (effective area: 0.5 cm^2) was mounted between the two middle compartments, while commercial CM-2 cation exchange membranes separated the outer compartments. Each compartment contained 100 mL of solution, with the electrode chamber filled with 0.3 $mol \cdot L^{-1}$ Na_2SO_4, the concentrate chamber with 0.01 $mol \cdot L^{-1}$ NaCl, and the dilution chamber with a 0.5 $mol \cdot L^{-1}$ mixed salt solution of NaCl/Na_2SO_4. To minimize concentration polarization, the solutions in all compartments were circulated at a flow rate of 50 $mL \cdot min^{-1}$ using a peristaltic pump. The system was operated for 1 hour at current densities of 6 $mA \cdot cm^{-2}$, and the ion concentrations in the concentrate chamber were determined by ion chromatography.

Ion permeation rate was calculated as follows:

$$J = \frac{V \times C_t}{A_m \times t} \tag{1}$$

where V refers to the effective volume of the permeate solution (L), C denotes the permeate concentration across the membrane ($mol \cdot L^{-1}$), A_m represents the effective area of the membrane (m^2), and t refers to the test time (h).

The permeation selectivity of the membranes was calculated according to the following equation:

$$S_M^N = \frac{J_N \times C_M}{C_N \times J_M} \tag{2}$$

where J_N and J_M refer to ion permeation rate ($mol \cdot m^{-2} \cdot h^{-1}$), C_M and C_N refer to ion concentrations in the dilution chamber ($mol \cdot L^{-1}$). All data collected were averaged over three parallel experiments, and standard deviations were calculated. N stands for monovalent anions and M for divalent anions.

Evaluation of the performance of the HOF-DAT-1 membrane in separating and concentrating NaCl

The performance of the HOF-DAT-1 membrane (effective area: 0.5 cm^2) was evaluated in two stages—separation of NaCl (Stage I) and concentration of NaCl (Stage II)—using an ED system configured with alternating layers of the HOF-DAT-1 membrane and a commercial CM-2 cation exchange membrane. In both stages, the electrode chambers were filled with 0.3 $mol \cdot L^{-1}$ NaCl (0.2 L). In Stage I, the concentration and dilution chambers contained 0.05 $mol \cdot L^{-1}$ NaCl (0.1 L) and 0.2 $mol \cdot L^{-1}$ NaCl/Na_2SO_4 (0.5 L), respectively. In Stage II, the solutions used in the concentration and dilution chambers were taken from the concentration chamber after 10 days of operation in Stage I (excluding the initial 0.05 $mol \cdot L^{-1}$ NaCl solution), with chamber volumes of 0.1 L and 3 L, respectively. To minimize concentration polarization, all solutions were circulated at a flow rate of 50 $mL \cdot min^{-1}$. The experiments were conducted at different current densities: 2, 6, and 10 $mA \cdot cm^{-2}$ in Stage I, and 30 $mA \cdot cm^{-2}$ in Stage II. The concentrations of Cl^- and SO_4^{2-} were quantified by ion chromatography.

The energy consumption (E, $kWh \cdot kg^{-1}$) for generating 1 kg of NaCl in the concentration chamber was calculated using the following equation:

$$E = \frac{\int_0^t (U \times I) dt}{(C_{Cl^-,c,t} \times V_{c,t} - C_{Cl^-,c,0} \times V_{c,0}) \times M_{NaCl}} \tag{3}$$

where $C_{Cl^-,c,0}$, $C_{Cl^-,c,t}$, $V_{c,0}$, and $V_{c,t}$ denote the concentration of Cl^- and the volume in the concentration chamber at the time of 0 and t, respectively; U, I, and t refer to the voltage (V), current (A), and operation time (h) of the power supply output, respectively; M_{NaCl} signifies the molar mass of NaCl (58.44 $g \cdot mol^{-1}$).

The current efficiency η_{Cl^-} was calculated using the following equation:

$$\eta_{Cl^-} = \frac{(C_{Cl^-,c,t} \times V_{c,t} - C_{Cl^-,c,0} \times V_{c,0}) \times Z \times F}{N \times \int_0^t Idt} \times 100\% \quad (4)$$

where $C_{Cl^-,c,0}$, $C_{Cl^-,c,t}$, $V_{c,0}$, and $V_{c,t}$ denote the concentration of Cl^- and the volume in the concentration chamber at the time of 0 and t, respectively; Z represents the ionic charge (Z = 1), F is the Faraday constant (F = 96485 $C \cdot mol^{-1}$), I and t refer to the current (A), and operation time (h) of the power supply output, respectively; N represents the number of membrane stack units (stage I: N = 2, stage II: N = 6).

The Cl^-/SO_4^{2-} selectivity was calculated using the following equation:

$$S = \frac{C_{Cl^-,c,t} \times V_{c,t} - C_{Cl^-,c,0} \times V_{c,0}}{C_{SO_4^{2-},c,t} \times V_{c,t} - C_{SO_4^{2-},c,0} \times V_{c,0}} \quad (5)$$

where $C_{Cl^-,c,0}$, $C_{Cl^-,c,t}$, $V_{c,0}$, and $V_{c,t}$ denote the concentration of Cl^- and the volume in the concentration chamber at the time of 0 and t, respectively; $C_{SO_4^{2-},c,0}$ and $C_{SO_4^{2-},c,t}$ refer to the concentration of SO_4^{2-} in the concentration chamber at the time of 0 and t, respectively; M_{Cl^-} and $M_{SO_4^{2-}}$ represent the relative molecular mass of Cl^- and SO_4^{2-} respectively.

The product purity (ρ) of NaCl in the concentration chamber was calculated using the following equation:

$$\rho = \frac{C_{c,t,NaCl} \times V_{c,t} \times M_{NaCl}}{C_{c,t,NaCl} \times V_{c,t} \times M_{NaCl} + C_{c,t,Na_2SO_4} \times V_{c,t} \times M_{Na_2SO_4}} \times 100\% \quad (6)$$

where $C_{c,t,NaCl}$, C_{c,t,Na_2SO_4}, and $V_{c,t}$ represent the concentrations of NaCl and Na_2SO_4 and the volume of the solution in the concentration chamber at time t, respectively; M_{NaCl} represents the molar mass of NaCl (58.44 $g \cdot mol^{-1}$), and $M_{Na_2SO_4}$ represents the molar mass of Na_2SO_4 (142.04 $g \cdot mol^{-1}$).

The commercial Neosepta® ACS anion selective membrane was tested and calculated using the same testing method.

The energy consumption per ton of wastewater treated $E_{Wastewater,\ m^{-3}}$ was calculated using the following equation:

$$E_{Wastewater,\ m^{-3}} = \frac{1000}{\frac{1000}{M_{NaCl}} \div (C_I \times V_I) \times V_{I,0}} \times E_I + \frac{1000}{\frac{1000}{M_{NaCl}} \div (C_{II} \times V_{II}) \times V_{II,0}} \times E_{II} \quad (7)$$

where C_I and C_{II} represent the sodium chloride concentrations in the concentrate after stage I and stage II, respectively; V_I and V_{II} are the volumes of the corresponding concentrate solutions from stage I and stage II, respectively; $V_{I,0}$ and $V_{II,0}$ denote the volumes of feed wastewater treated in stage I and stage II, respectively; E_I and E_{II} indicate the energy consumption per kilogram of NaCl produced in stage I and stage II, respectively. M_{NaCl} is the molar mass of NaCl (58.44 $g \cdot mol^{-1}$).

Data availability

The authors confirm that the data supporting the findings of this study are available within the article and its supplementary information. All data are available from the corresponding author upon request.

References

1. Xie, X., Chen, C., Zhang, N., Tang, Z.-R., Jiang, J. & Xu, Y.-J. Microstructure and surface control of MXene

films for water purification. *Nat. Sustainability* **2**, 856-862 (2019).

2. Bolisetty, S. & Mezzenga, R. Amyloid–carbon hybrid membranes for universal water purification. *Nat. Nanotechnol.* **11**, 365-371 (2016).
3. Huang, J., et al. Sustainable nanofiltration membranes enable ultrafast water purification. *Nat. Water* **3**, 1048-1056 (2025).
4. Wang, Y., Lian, T., Tarakina, N. V., Yuan, J. & Antonietti, M. Lamellar carbon nitride membrane for enhanced ion sieving and water desalination. *Nat. Commun.* **13**, 7339 (2022).
5. Zhang, X., et al. Electrodialytic crystallization to enable zero liquid discharge. *Nat. Water* **1**, 547-554 (2023).
6. Xu, X., et al. Nanofiltration membranes with ultra-high negative charge density for enhanced anion sieving and removal of organic micropollutants. *Nat. Water* **3**, 704-713 (2025).
7. Zhao, C., et al. Polyamide membranes with nanoscale ordered structures for fast permeation and highly selective ion-ion separation. *Nat. Commun.* **14**, 1112 (2023).
8. Jentsch, T. J., Stein, V., Weinreich, F. & Zdebik, A. A. Molecular structure and physiological function of chloride channels. *Physiol. Rev.* **82**, 503-568 (2002).
9. Miller, C. CLC chloride channels viewed through a transporter lens. *Nature* **440**, 484-489 (2006).
10. Leisle, L., et al. Backbone amides are determinants of Cl^- selectivity in CLC ion channels. *Nat. Commun.* **13**, 7508 (2022).
11. Paulino, C., Kalienkova, V., Lam, A. K. M., Neldner, Y. & Dutzler, R. Activation mechanism of the calcium-activated chloride channel TMEM16A revealed by cryo-EM. *Nature* **552**, 421-425 (2017).
12. Dutzler, R., Campbell, E. B. & MacKinnon, R. Gating the selectivity filter in CLC chloride channels. *Science* **300**, 108-112 (2003).
13. Abraham, J., et al. Tunable sieving of ions using graphene oxide membranes. *Nat. Nanotechnol.* **12**, 546-550 (2017).
14. Kang, Y., et al. Nanoconfinement enabled non-covalently decorated MXene membranes for ion-sieving. *Nat. Commun.* **14**, 4075 (2023).
15. Mo, R.-J., et al. Regulating ion affinity and dehydration of metal-organic framework sub-nanochannels for high-precision ion separation. *Nat. Commun.* **15**, 2145 (2024).
16. Meng, Q.-W., et al. Guanidinium-based covalent organic framework membrane for single-acid recovery. *Sci. Adv.* **9**, eadh0207 (2023).
17. Meng, Q.-W., et al. Optimizing selectivity via membrane molecular packing manipulation for simultaneous cation and anion screening. *Sci. Adv.* **10**, eado8658 (2024).
18. Yan, T. & Liu, J. Transmembrane ion channels: from natural to artificial systems. *Angew. Chem. Int. Ed.* **64**, e202416200 (2025).
19. Wu, Y., et al. 2D molecular sheets of hydrogen-bonded organic frameworks for ultrastable sodium-ion storage. *Adv. Mater.* **33**, 2106079 (2021).
20. Chen, C., Shen, L., Lin, H., Zhao, D., Li, B. & Chen, B. Hydrogen-bonded organic frameworks for membrane separation. *Chem. Soc. Rev.* **53**, 2738-2760 (2024).
21. Shang, X., et al. Chiral self-sorted multifunctional supramolecular biocoordination polymers and their applications in sensors. *Nat. Commun.* **9**, 3933 (2018).
22. Feng, S., et al. Fabrication of a hydrogen-bonded organic framework membrane through solution processing for pressure-regulated gas separation. *Angew. Chem. Int. Ed.* **59**, 3840-3845 (2020).

23. Yin, Q., et al. Hydrogen-bonded organic frameworks in solution enables continuous and high-crystalline membranes. *Nat. Commun.* **15**, 634 (2024).
24. Wang, Y., Song, L.-N., Wang, X.-X., Wang, Y.-F. & Xu, J.-J. Hydrogen-bonded organic frameworks-based electrolytes with controllable hydrogen bonding networks for solid-state lithium batteries. *Angew. Chem. Int. Ed.* **63**, e202401910 (2024).
25. Wang, J., et al. In situ assembly of hydrogen-bonded organic framework on metal–organic framework: an effective strategy for constructing core–shell hybrid photocatalyst. *Adv. Sci.* **9**, 2204036 (2022).
26. Meng, W., et al. Three-dimensional cationic covalent organic framework membranes for rapid and selective lithium extraction from saline water. *Nat. Water* **3**, 191-200 (2025).
27. Park, H. B., Kamcev, J., Robeson, L. M., Elimelech, M. & Freeman, B. D. Maximizing the right stuff: The trade-off between membrane permeability and selectivity. *Science* **356**, eaab0530 (2017).
28. Wang, H., et al. Covalent organic framework membranes for efficient separation of monovalent cations. *Nat. Commun.* **13**, 7123 (2022).
29. Xu, R., Kang, Y., Zhang, W., Zhang, X. & Pan, B. Oriented UiO-67 metal–organic framework membrane with fast and selective lithium-ion transport. *Angew. Chem. Int. Ed.* **61**, e202115443 (2022).
30. Hong, Z., et al. Rigid and flexible coupled micropore membranes enabling ultra-efficient anion separation. *AlChE J.* **71**, e18803 (2025).
31. Lu, D., et al. Impact of charge homogeneity on ion selectivity in polyamide membranes. *Nat. Water* **3**, 978-991 (2025).
32. Zhang, Y., et al. Ice-confined synthesis of highly ionized 3D-quasilayered polyamide nanofiltration membranes. *Science* **382**, 202-206 (2023).
33. Irfan, M., Ge, L., Wang, Y., Yang, Z. & Xu, T. Hydrophobic side chains impart anion exchange membranes with high monovalent–divalent anion selectivity in electrodialysis. *ACS Sustainable Chem. Eng.* **7**, 4429-4442 (2019).
34. Xu, T., et al. Scalable and interfacial gap-free mixed matrix membranes for efficient anion separation. *AlChE J.* **70**, e18242 (2024).
35. Liao, J., Yu, X., Pan, N., Li, J., Shen, J. & Gao, C. Amphoteric ion-exchange membranes with superior mono-/bi-valent anion separation performance for electrodialysis applications. *J. Membr. Sci.* **577**, 153-164 (2019).
36. Liao, J., et al. Monovalent anion selective anion-exchange membranes with imidazolium salt-terminated side-chains: Investigating the effect of hydrophobic alkyl spacer length. *J. Membr. Sci.* **599**, 117818 (2020).
37. Li, J., et al. The endowment of monovalent anion selectivity and antifouling property to cross-linked ion-exchange membranes by constructing amphoteric structure. *Sep. Purif. Technol.* **328**, 125104 (2024).
38. Xiao, X., et al. Anion permselective membranes with chemically-bound carboxylic polymer layer for fast anion separation. *J. Membr. Sci.* **614**, 118553 (2020).
39. Li, M., Li, W., Zhang, X., Wu, C., Han, X. & Chen, Y. Polyvinyl alcohol-based monovalent anion selective membranes with excellent permselectivity in selectrodialysis. *J. Membr. Sci.* **620**, 118889 (2021).
40. Wang, C., Pan, N., Liao, J., Ruan, H., Sotto, A. & Shen, J. Effect of microstructures of side-chain-type anion exchange membranes on mono-/bivalent anion permselectivity in electrodialysis. *ACS Appl. Polym. Mater.* **3**, 342-353 (2021).
41. Lejarazu-Larrañaga, A., Zhao, Y., Molina, S., García-Calvo, E. & Van der Bruggen, B. Alternating current enhanced deposition of a monovalent selective coating for anion exchange membranes with antifouling properties. *Sep. Purif. Technol.* **229**, 115807 (2019).

42. Liao, J., et al. Amphoteric blend ion-exchange membranes for separating monovalent and bivalent anions in electrodialysis. *Sep. Purif. Technol.* **242**, 116793 (2020).
43. Liao, J., et al. Long-side-chain type imidazolium-functionalized fluoro-methyl poly(arylene ether ketone) anion exchange membranes with superior electrodialysis performance. *J. Membr. Sci.* **574**, 181-195 (2019).
44. Yang, H., et al. Poly(alkyl-biphenyl pyridinium) anion exchange membranes with a hydrophobic side chain for mono-/divalent anion separation. *Ind. Chem. Mater.* **1**, 129-139 (2023).
45. Li, J., et al. Revolutionary MOF-enhanced anion exchange membrane for precise monovalent anion separation through structural optimization and doping. *Desalination* **576**, 117352 (2024).
46. Pan, J., Ding, J., Zheng, Y., Gao, C., Van der Bruggen, B. & Shen, J. One-pot approach to prepare internally cross-linked monovalent selective anion exchange membranes. *J. Membr. Sci.* **553**, 43-53 (2018).
47. Goel, P., E, B., Mandal, P., Shahi, V. K., Bandyopadhyay, A. & Chattopadhyay, S. Di-quaternized graphene oxide based multi-cationic cross-linked monovalent selective anion exchange membrane for electrodialysis. *Sep. Purif. Technol.* **276**, 119361 (2021).
48. Jiang, C., et al. Fouling deposition as an effective approach for preparing monovalent selective membranes. *J. Membr. Sci.* **580**, 327-335 (2019).
49. Tekinalp, Ö., Zimmermann, P., Burheim, O. S. & Deng, L. Designing monovalent selective anion exchange membranes for the simultaneous separation of chloride and fluoride from sulfate in an equimolar ternary mixture. *J. Membr. Sci.* **666**, 121148 (2023).
50. Afsar, N. U., et al. In-situ interfacial polymerization endows surface enrichment of -COOH groups on anion exchange membranes for efficient Cl^-/SO_4^{2-} separation. *J. Polym Sci.* **60**, 3022-3034 (2022).
51. Ahmad, M., Tang, C., Yang, L., Yaroshchuk, A. & Bruening, M. L. Layer-by-layer modification of aliphatic polyamide anion-exchange membranes to increase Cl^-/SO_4^{2-} selectivity. *J. Membr. Sci.* **578**, 209-219 (2019).
52. You, X., et al. Charged nanochannels in covalent organic framework membranes enabling efficient ion exclusion. *ACS Nano* **16**, 11781-11791 (2022).
53. Lu, C., et al. Dehydration-enhanced ion-pore interactions dominate anion transport and selectivity in nanochannels. *Sci. Adv.* **9**, eadf8412 (2023).
54. Richards, L. A., Richards, B. S., Corry, B. & Schäfer, A. I. Experimental energy barriers to anions transporting through nanofiltration membranes. *Environ. Sci. Technol.* **47**, 1968-1976 (2013).
55. Zhou, X., et al. Intrapore energy barriers govern ion transport and selectivity of desalination membranes. *Sci. Adv.* **6**, eabd9045 (2020).
56. Richards, L. A., Schäfer, A. I., Richards, B. S. & Corry, B. Quantifying barriers to monovalent anion transport in narrow non-polar pores. *Phys. Chem. Chem. Phys.* **14**, 11633-11638 (2012).
57. Chandra, A. Effects of ion atmosphere on hydrogen-bond dynamics in aqueous electrolyte solutions. *Phys. Rev. Lett.* **85**, 768-771 (2000).
58. Liu, M.-L., et al. Microporous membrane with ionized sub-nanochannels enabling highly selective monovalent and divalent anion separation. *Nat. Commun.* **15**, 7271 (2024).
59. Epsztein, R., DuChanois, R. M., Ritt, C. L., Noy, A. & Elimelech, M. Towards single-species selectivity of membranes with subnanometre pores. *Nat. Nanotechnol.* **15**, 426-436 (2020).
60. Ries, L., et al. Enhanced sieving from exfoliated MoS_2 membranes via covalent functionalization. *Nat. Mater.* **18**, 1112-1117 (2019).
61. Kitto, D., Espinoza, C., Díaz, J. C., Zamora, J. & Kamcev, J. Fast and selective ion transport in ultrahigh-charge-

density membranes. *Nat. Chem. Eng.* **2**, 252-260 (2025).

62. Feng, L., Tian, B., Zhu, M. & Yang, M. Current progresses in the analysis, treatment and resource utilization of industrial waste salt in China: a comprehensive review. *Resour. Conserv. Recycl.* **217**, 108224 (2025).
63. Wang, T., Wang, H., Chen, J., Wang, Z., Dai, R. & Wang, Z. Low-salt-rejection reverse osmosis membranes decrease energy consumption and economic cost in a wastewater zero liquid discharge system. *Desalination* **620**, 119629 (2026).
64. Zhang, X., Wang, X., Wang, Y., Li, C., Feng, H. & Xu, T. Production of yellow iron oxide pigments by integration of the air oxidation process with bipolar membrane electrodialysis. *Ind. Eng. Chem. Res.* **53**, 1580-1587 (2014).
65. He, D., et al. Bipolar membrane electrodialysis with isolation chamber enables high-purity LiOH production with ordinary membranes. *AlChE J.* **71**, e18674 (2025).

Acknowledgements

This work was supported by the National Key R&D Program of China (No. 2022YFB3805100 [J. R.]), and the National Natural Science Foundation of China (No. 22278105 [J. R.]). The computation is completed on the HPC Platform of Hefei University of Technology. The analysis work of this article was partially carried out at the Instrumental Analysis Center, Hefei University of Technology.

Author contributions

J.R., P.Z., and T.X. conceived the idea and designed the experiments. S.Z. carried out the material synthesis, characterization, and performance tests. Z.W. and C. F. performed the MD simulations. X. Z, G. L., Q. Z., and P. C. contributed to the data curation and investigation. S.Z. and Z.W. performed the data analysis. All coauthors discussed the results. S.Z. and P. Z. wrote the manuscript. J.R., P.Z., and T.X. revised the manuscript.

Competing interests

The authors declare no competing interests.

Fig. 1 | Design of HOF membranes with biomimetic chloride ion channels. a, Schematic illustration of the biological CLC Cl^- channel. **b**, Schematic illustration of the biomimetic Cl^- channel structure constructed by HOF. **c**, Digital photograph and molecular structure of the HOF-DAT membrane. **d**, Pore structure diagram of HOF-DAT membrane in different directions. **e**, Cross-section SEM images of HOF-DAT membrane. **f**, XRD patterns of HOF-DAT membrane and its powder form. **g**, HR-TEM image of the HOF-DAT membrane. Inset: the inverse Fast Fourier Transform lattice image of the area in red. **h**, N_2 adsorption isotherms of HOF-DAT membrane at 77 K and Horvath-Kawazoe pore size distributions.

Fig. 2 | Anion separation performance of HOF membranes. a, Schematic diagram of a diffusion dialysis (DD) unit. b, Cl^- permeation rate and Cl^-/SO_4^{2-} selectivity of HOF-DAT membranes in 0.5 $mol \cdot L^{-1}$ $NaCl/Na_2SO_4$ binary-salt solution. c, Ion permeation rate and selectivity of the HOF-DAT-1 membrane in different mixed salt solutions. d, Cyclic stability of the HOF-DAT-1 membrane. e, Comparison of Cl^-/SO_4^{2-} separation performances between HOF-DAT membranes and literature-reported membranes[16, 17, 31, 32, 33, 34, 35, 36, 37, 38, 39, 40, 41, 42, 43, 44, 45, 46, 47, 48, 49, 50, 51]. f, Radar plot comparing the comprehensive characteristics of the HOF-DAT-1 and reported

membranes[16, 17, 35, 52] (The data acquired for the HOF-DAT-1 membrane operating in the DD mode were employed as a benchmark). g, Comparisons of the ion transport energy barrier of the HOF-DAT-1 membrane with literature-reported membranes and channels across varying pore diameters[53, 54, 55, 56]. Error bars represent the mean ± SD, n = 3.

Fig. 3 | Mechanism of anion transport and separation. a, XRD patterns of the HOF-DAT-1 membrane upon immersion in solutions containing different anions. **b**, Anion transport-induced pore size changes in the HOF-DAT membrane. Insert: schematic of the pore structure, where for descriptive purposes, the parameters a and b represent the pore dimensions of W_1 along different directions, while c and d represent those of W_2. **c-f**, Snapshots of the first hydration shell of the ions from a 50 ns MD simulation at 300 K: Cl^- and SO_4^{2-} in bulk solution and HOF-DAT. Water molecules in the first hydration shell are shown in Corey-Pauling-Koltun (CPK) representation, with the remaining waters as licorice. HOF-DAT are shown in licorice representation, with cyan, red, navy, and white representing carbon, oxygen, nitrogen, and hydrogen atoms, respectively. For clarity, hydrogen atoms from HOF-DAT's NH_2 groups participating in the first hydration shell are represented by white spheres. Ions are shown as van der Waals (vdW) spheres, with green for chlorine (Cl^-) and yellow for sulfur (in SO_4^{2-}). **g**, Hydrogen coordination number in the first hydration shell of the ions: provided by water molecules (H_W) in bulk solution, and by both water molecules (H_W) and NH_2 groups (H_N) in HOF-DAT (The coordination number reported here is defined based solely on spatial proximity, considering hydrogen atoms located within the first hydration shell of the ion). **h**, Hydrogen bond lifetime of Cl^--H and SO_4^{2-}-H in bulk and HOF-DAT.

Fig. 4 | Demonstration of high-salinity wastewater valorization via ED. a, Schematic diagram of the two-stage ED process. The performance of the ED cell with HOF-DAT-1 was evaluated, with the Neosepta® ACS membrane as the control sample. **b**, XRD pattern of the NaCl product collected after the ED assembled with HOF-DAT-1, confirming its high purity by a complete match with the standard reference. The inset shows a photograph of the final NaCl products. **c**, **d,** Evolution of NaCl and Na_2SO_4 concentrations in the concentrate during two-stage ED: (**c**) first-stage at 6 $mA \cdot cm^{-2}$ for separation, and (**d**) second-stage at 30 $mA \cdot cm^{-2}$ for concentration. **e**, Evolution of NaCl purity in the concentrate during two-stage ED. **f**, Radar plot comparing the comprehensive characteristics of HOF-DAT-1 and Neosepta® ACS membranes.

Editorial Summary

Replicating the functional architecture of biological ion channels in synthetic membranes remains challenging. Here the authors design an ultramicroporous hydrogen-bonded organic framework membrane that structurally emulates the CLC chloride filter.

Peer review information: *Nature Communications* thanks Liguo Shen and the other, anonymous, reviewers for their contribution to the peer review of this work. A peer review file is available.